

# Delivery Pathway Regulation of 3',3''-Bis-Peptide-siRNA Conjugate via Nanocarrier Architecture Engineering

Jing Sun,<sup>1,2</sup> Chong Qiu,<sup>1,2</sup> Yiping Diao,<sup>1</sup> Wei Wei,<sup>1</sup> Hongwei Jin,<sup>1</sup> Yi Zheng,<sup>1</sup> Jiancheng Wang,<sup>1</sup> Lihe Zhang,<sup>1</sup> and Zhenjun Yang<sup>1</sup>

<sup>1</sup>State Key Laboratory of Natural and Biomimetic Drugs, School of Pharmaceutical Sciences, Peking University, Beijing 100191, China

**Small interfering RNA (siRNA) has been continuously explored for clinical applications. However, neither nanocarriers nor conjugates have been able to remove the obstacles. In this study, we employed a combined nanochemistry strategy to optimize its delivery dilemma, where different interactions and assembly modes were cooperatively introduced into the forming process of siRNA/lipids nanoplexes. In the nanoplexes, the 3',3''-bis-peptide-siRNA conjugate (pp-siRNA) and gemini-like cationic lipids (CLDs) were employed as dual regulators to improve their bio-behavior. We demonstrated that the “cicada pupa”-shaped nanoplexes of MT-pp-siRNA/CLDs (MT represented the mixed two-phase method) exhibited more compact multi-sandwich structure (~25 layers), controllable size (~150 nm), and lower zeta potential (~22 mV) than other comparable nanoplexes and presented an increased siRNA protection and stability. Significantly, the nanoplex was internalized into melanoma cells by almost caveolae-mediated endocytosis and macropinocytosis (~99.46%), and later reduced/avoided lysosomal degradation. Finally, the nanoplex facilitated the silencing of mRNA of the mutant B-Raf protein (down by ~60%). In addition, pp-siRNA had a high intracellular sustainability, a significantly prolonged circulating time, and accumulation in tumor tissues *in vivo*. Our results have demonstrated that the combined approach can improve the intracellular fate of siRNA, which opens up novel avenues for efficient siRNA delivery.**

## INTRODUCTION

RNAi technologies are currently emerging as the major drug discovery approaches of the most promising drug candidate molecules.<sup>1–3</sup> However, intrinsic drawbacks (e.g., instability, cell impermeability, and off-target effect) have impeded the application of small interfering RNA (siRNA) in clinic.<sup>4,5</sup> Countless types of non-viral vectors have blossomed to improve the above-mentioned dilemma.<sup>6–8</sup>

As nanocarriers with the greatest potential,<sup>9–11</sup> cationic liposomes still need to overcome several defects. When using the AT method (thin film hydration),<sup>12,13</sup> most liposomes (as per our previous study) merely adsorbed siRNA onto their surfaces via electrostatic forces. These

nanoplexes cannot provide siRNA a better protection from RNase degradation in the transport process. Moreover, the relatively stochastic and incompact self-assembly process may cause fluctuation of these nanoplexes' property parameters (sizes, zeta potential, morphology, etc.), which disturbs the accuracy of biological evaluation.<sup>14</sup> To improve the aforementioned problems, several delivery systems were attempted and indeed presented significant transfection efficiency, such as the multifunctional nanodevices, for example, multifunctional envelope-type nanodevices (MENDs),<sup>15,16</sup> liposome-polycation-DNA particle (LPD),<sup>17,18</sup> or other core-shell nanoparticles.<sup>19,20</sup>

In our previous studies,<sup>21,22</sup> a redox-responsive cationic lipid (CLD; Figure 1) was devised for siRNA delivery, which displayed efficient target mRNA inhibition and low cytotoxicity *in vitro*. Furthermore, mechanistic research uncovered that disulfide-bridge played a key role in promoting the siRNA release. Recently, our laboratory designed a series of peptide-siRNA conjugates.<sup>23–25</sup> Subsequent results revealed that peptide conjugated at the 3' terminus of the sense strand can improve siRNA resistance from ribozyme and strand selection for loading the guide strand to RISC (RNA-induced silencing complex), which provided a direction of siRNA design for efficient silencing with low off-target effect. Furthermore, based on the conjugation feasibility at the 3' terminus of the guide strand, the 3',3''-bis-peptide-siRNA conjugate (pp-siRNA) was obtained, which demonstrated a prolonged circulation time and better treatment results in nude mice.<sup>26</sup> With 3'-terminal peptide-siRNA conjugates, an extra-hydrophobic peptide at the 3' terminus of the guide strand may alter the preparation of nanostructures, then directly affect the encapsulation status, intracellular fates (transmembrane pathway, distribution, and

Received 20 July 2017; accepted 7 November 2017;  
<https://doi.org/10.1016/j.omtn.2017.11.002>.

<sup>2</sup>These authors contributed equally to this work.

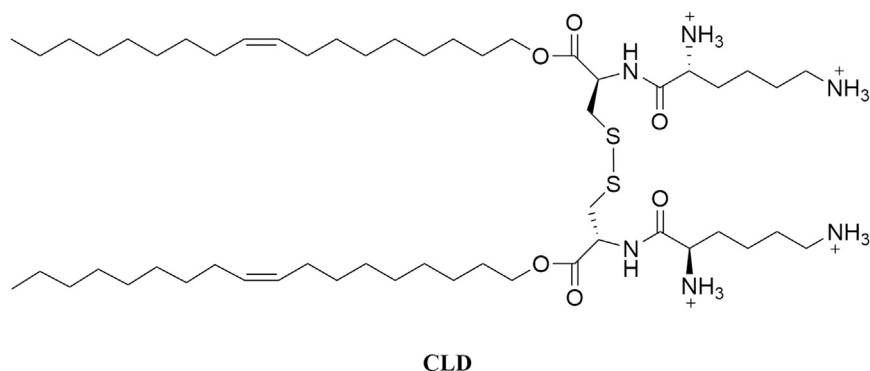
**Correspondence:** Zhenjun Yang, State Key Laboratory of Natural and Biomimetic Drugs, School of Pharmaceutical Sciences, Peking University, 38 Xueyuan Road, Beijing 100191, China.

**E-mail:** yangzj@bjmu.edu.cn

**Correspondence:** Jiancheng Wang, State Key Laboratory of Natural and Biomimetic Drugs, School of Pharmaceutical Sciences, Peking University, 38 Xueyuan Road, Beijing 100191, China.

**E-mail:** wang-jc@bjmu.edu.cn



**Figure 1. Chemical Structure of CLD**

The H-shaped gemini-like CLD that is composed of two natural alkaline lysine heads and two biocompatible oleyl alcohol tails with a bridge of redox-responsive disulfide bond.

degradation), finally resulting in the distinct silencing effect. Melanoma is a malignant tumor of melanocytes, which cannot be effectively treated until now. It has been confirmed that the B-RAF mutation, which activates the downstream extracellular regulated protein kinase (ERK)1/2 pathways, exists in most melanoma patients (~80%) and provokes the tumor cell proliferation, migration, and so on. The siRNA sequence of siMB3 was targeted against mutant B-RAF mRNA.<sup>27</sup>

To promote the siMB3 bio-effect in the melanoma model, we constructed the pp-siRNA/CLD delivery system using a conventional assembly process (thin-film hydration, AT method). Our hypothesis was that the bis-peptides at the 3' termini of pp-siRNA can be inserted into the hydrophobic region of liposomes, which can influence or regulate the architecture of nanocarriers via extra interaction with the tail chain of CLD lipids, thereby inducing a significant improvement of the nanoplexes' bio-behaviors. Nevertheless, in the AT process, the contact areas may be limited for the phospholipid tails arranged into the liposomal bilayers, with inadequate extra-hydrophobic interaction between pp-siRNA and CLDs. Thus, to maximize the bis-peptides' regulating effect in the assembly process, another assembly strategy, called the mixed two-phase (MT) method, was applied. We supposed that the MT nanoplexes of pp-siRNA/CLDs could encapsulate more pp-siRNA inside compared with those of the AT method and had a stronger interaction between siRNA and CLDs. These distinct constitutive properties may give the MT siRNA/CLDs nanoplexes a better stability and siRNA protection with improved cellular uptake and gene knockdown. Using siRNA as another control, the different assembly processes were elaborated to interpret the reasons for enhanced stability and unique intracellular fate of nanoplexes of pp-siRNA/CLDs. In addition, the advantages of the novel 3',3''-bis-peptide-siRNA conjugate were also confirmed by the results of the assembly process, endosomal transport assay and fluorescence resonance energy transfer (FRET) assay, compared with the 3'-peptide-siRNA conjugates, which were widely reported in the siRNA conjugation field.

## RESULTS

### Confirmation of siMB3 Sequences

Identifications of all single strands after purification were confirmed using MALDI-TOF-mass spectrometry (MS) (Tables 1

and S1; Figure S3). The detailed protocols can be seen in the Supplemental Information.

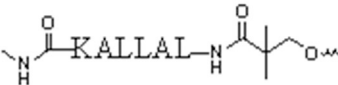
### Characteristics of Supramolecular Assemblies

Four nanoplexes of pp-siRNA/CLDs and siRNA/CLDs were obtained via both the AT and the MT preparation, in which the conditions, such as transmission electron microscopy (TEM), dynamic light scattering (DLS), small-angle X-ray scattering (SAXR), and molecular dynamic simulation (MDS), were screened and optimized (Figure S4). As seen from Table 2 and Figures 2A and 2C, all nanoplexes can effectively form uniform nanostructures at N/P = 5/1, with a size range between ~80 and ~150 nm. Notably, N/P = 5/1 was selected because our data showed the optimal parameters of four nanoplexes via the multi-factors screening test, which is presented in the Supplemental Information. For the AT preparation, the pp-siRNA/CLDs nanoplexes clearly shared lower zeta potentials ( $+26.4 \pm 1.50$  mV) and larger sizes ( $94.1 \pm 2.96$  nm) compared with the siRNA/CLDs nanoplexes with a zeta potential of  $+36.6 \pm 1.97$  mV and hydrodynamic size of  $86.8 \pm 1.90$  nm. Moreover, the similar decrease in zeta potentials was also observed in the MT nanoplexes. In addition, the sizes of nanoplexes in the MT preparation (~150 nm) were significantly larger than those of the AT nanoplexes (~90 nm).

Using TEM, the morphology showed that the AT nanoplexes were uniform spherical vesicles (Figures 2Aa and 2Ab). However, the MT nanoplexes were distinct assemblies composed of filamentous nanoribbons. The nanoplexes of pp-siRNA/CLDs formed the ellipsoid-shaped nanostructures (Figure 2Ac). Meanwhile, the nanoplexes of siRNA/CLDs were observed as acalphe-like formations (Figure 2Ad). In the SAXR analysis (Figure 2B), all of the nanoplexes displayed a single peak, which implied that they were comprised of periodically repeating units. There was a peak shift among these nanoplexes, which displayed the different compression degrees between pp-siRNA/siRNA and CLDs. Nevertheless, the diametral parameters of the units were evidently different based on data analysis, specifically 4.96 nm (CLDs), 5.60 nm (MT-siRNA/CLDs), 5.56 nm (MT-pp-siRNA/CLDs), 5.73 nm (AT-siRNA/CLDs), and 5.95 nm (AT-pp-siRNA/CLDs).

Two nanoplexes of the 3'-peptide-siRNA conjugates (3'-pS-siRNA and 3'-pAs-siRNA)/CLDs, which were also prepared via the MT method at the ratio of N/P = 5/1, were observed using TEM (Figures 2Ae and 2Af). Both of them displayed different morphologies compared with those of pp-siRNA and siRNA. These nanoplexes were apt to accumulate mutually and formed irregular

**Table 1. Abbreviations for the Corresponding Samples**

Entry	Name	Sequence and/or chemical structure	Function
1	siMB3	S: 5'-GCUACAGAGAAAUCUCGAUdt-3' As: 5'-AUCGAGAUUUCUCUGUAGCdt-3'	Both
2	p(Peptidyl-)	 linked with the 3'-terminus of RNA	Both pp-siMB3 and siMB3 were targeted for
3	pAs-siMB3	Peptide conjugate at the 3'-terminal of the antisense strand of siMB3	B-RAF mRNA in
4	pS-siMB3	Peptide conjugate at the 3'-terminal of the sense strand of siMB3	melanoma A375 cells
5	pp-siMB3	Peptide conjugate at both 3'-terminals of siMB3	

supramolecular clusters. These results further demonstrated that the bis-peptide at the terminus of pp-siRNA played a key role in regulating the assembly process between siRNA and CLDs, which cannot be perfectly substituted by the 3'-p-siRNA conjugates.

#### Stability and Cytotoxicity of the Nanoplexes

The results from gel retardation assay (Figure 3A) confirmed that both pp-siRNAs and siRNAs can be completely packaged by cationic CLDs at the N/P ratio of 5/1 and released out adequately by the anionic substance (1% SDS) displacement, which implied that intracellular siRNAs can be integrally released from the nanoplexes. As shown in Figure 3B, approached with fetal bovine serum (FBS), four nanoplexes were degraded at different degrees in the same preparation, pp-siRNAs were better protected than naked siRNAs. Moreover, the MT nanoplexes displayed an advantage in siRNA protection, compared with the AT nanoplexes. The results in Figure 3C showed that, in the same preparation, pp-siRNA had a better stability against heparin displacement than siRNA. Moreover, the MT nanoplexes displayed an advantage compared with the AT nanoplexes.

Because the cationic nanoparticle-mediated cell membrane damage is a potential safety concern, a hemolysis assay was used to evaluate the biosafety of these nanoplexes. As seen from Figure 3D, at the concentration of 100 nM siRNA (which is equivalent to the nanoplex con-

centration of the subsequent drug dose), the hemolysis rate of all nanoplexes was <2%, which meant that nanoplexes had good biocompatibility. Besides, at an approximately 150 nM dose, the rate of MT-siRNA/CLDs nanoplexes was higher up to 8%, which may be because of the increased immunogenicity of their larger sizes compared with AT formations and higher potentials than MT-pp-siRNA/CLDs. The sharp increase of hemolysis implied that the nanoplexes of MT-siRNA/CLDs may have a higher cytotoxicity than others. Hence, the maximum concentration was chosen at 100 nM. In addition, all nanoplexes presented a favorable stability for 2 days at the concentrations of 200 nM (Figure 3E), as well as that of 5% glucose.

#### Uptake and Endocytosis Dissection

Cy3-labeled pp-siRNA/siRNA was used as a fluorescent indicator to monitor the internalization of nanoplexes in A375 cells. Fluorescence intensity (Figure 4A) was detected via flow cytometry (FCM), and the distribution was determined (Figure 4B) using a confocal fluorescence microscope. In Figure 4, the observed fluorescence intensity of the Cy3-labeled pp-siRNA/CLDs nanoplexes was higher than that of siRNA/CLDs in the same preparation, at both the 4<sup>th</sup> and 6<sup>th</sup> hr. This uptake difference between pp-siRNA and siRNA may suggest that these nanoplexes may enter into cells through distinct cellular pathways.

**Table 2. Characteristics of the Four Nanoplexes**

Prescriptions	Mean Particle Size (d, nm)	Polydispersity Index (PDI)	Zeta Potential (mV)
AT-pp-siMB3/CLDs	94.1 ± 2.96	0.20 ± 0.046	+26.4 ± 1.50
AT-siMB3/CLDs	86.8 ± 1.90	0.21 ± 0.012	+36.6 ± 1.97
MT-pp-siMB3/CLDs	150 ± 7.60	0.14 ± 0.063	+22.1 ± 3.14
MT-siMB3/CLDs	151 ± 12.5	0.17 ± 0.016	+28.0 ± 2.46

To elucidate the endocytic pathways involved in the uptake of nanoplexes, we employed a number of inhibitors that were widely used to identify clathrin-dependent endocytosis (CME), caveolae-mediated endocytosis (CvME), macropinocytosis, and ATP-dependent endocytosis (Table S2). Because the effect of the inhibitors is dose dependent and can compromise the vital cellular processes at high concentrations, the cytotoxic effect of the inhibitors was assessed over a concentration range (Figure S5). The final concentrations were defined by >80% cellular viability rates. As seen in Figure 5A, amiloride evidently reduced the uptake of MT nanoplexes by approximately 50%, especially MT-pp-siRNA/CLDs, but otherwise had minimal effect on the uptake of AT nanoplexes. Amantadine and chlorpromazine influenced the uptake of AT nanoplexes more than MT nanoplexes. Therefore, the uptake of AT-siRNA/CLDs was clearly reduced by 50% (amantadine) and 20% (chlorpromazine).  $\beta$ -cyclodextrin ( $\beta$ -CD) can significantly decrease the uptake of all nanoplexes by 50% at the concentration of 5 mM, except for that of AT-siRNA/CLDs. Genistein and nystatin markedly reduced the uptake of AT-pp-siRNA/CLD nanoplexes, but only at a high concentration of 40  $\mu$ g/mL. The uptake of all nanoplexes was drastically reduced by ~50% under the condition of both 0.1%  $\text{NaN}_3$  and 4°C, especially for the AT nanoplexes.

To complement the quantitative results from FCM, we generated qualitative information on the endocytosis pathways of nanoplexes using confocal laser scanning microscopy (CLSM). Figure 5C is the CLSM images of A375 cells transfected with the nanoplexes of Cy5-labeled pp-siRNA/siRNA (red) and fluorescence-labeled channel markers such as transferrin, cholera toxin B, and dextran (green). The AT nanoplexes appeared to be mainly co-localized with transferrin and cholera toxin B (white arrows), in which the shared patterns between the nanoplexes of pp-siRNA/CLDs and cholera toxin B were more than those of siRNA/CLDs. Although two MT nanoplexes were predominantly co-localized with two markers (cholera toxin B and dextran), the co-localization of MT-pp-siRNA/CLDs with transferrin was rarely observed compared with that of MT-siRNA/CLDs.

To summarize these results of the CLSM images (Figure 5C), FCM (Figure 5A), and fluorescence microscopy (Figure 5B), we drew a channel ratio picture (Figure 5D) that was formed by selecting an appropriate concentration in each inhibitor (amiloride 0.5 mM, nystatin 40  $\mu$ g/mL, genistein 40  $\mu$ g/mL, chlorpromazine 5  $\mu$ g/mL, amantadine 1 mM), setting the sum of inhibition rate of all inhibitors

as 100% to calculate the proportional value of three main uptake channels. The results showed that the proportion of the CvME-mediated endocytosis in the uptake of pp-siRNA was larger than that of siRNA. Moreover, the higher ratio of macropinocytosis was observed in the MT nanoplex uptake compared with that of AT nanoplexes.

### Endosome Transportation

Early/late endosomes of the MT nanoplexes of 3'-pS/pAs-siRNA conjugates with CLDs were observed in transfected cells after 0.5-, 0.75-, 1-, and 1.5-hr points using CLSM (Figure 6A), and Pearson's correlation was measured (Figure 6D). Several detailed results were listed in the Supplemental Information (section 9). Yellow dots (co-localization) were highlighted. At the 0.5-hr point, the nanoplexes of pp-siRNA/CLDs and 3'-pAs-siRNA/CLDs were rapidly generated; as time went by, the yellow dots gradually appeared until the 1.5-hr point. In addition, the intracellular distribution of nanoplexes of 3'-pS-siRNA/CLDs has few co-localizations during this time. These results displayed that the nanoplexes of pp-siRNA/CLDs were superior to those of siRNA/CLDs, which implied that they may escape the intracellular acidified degradation process.

### Lysosome Escape

The CLSM images of intracellular distribution (Figures 6B and 6F) were revealed using the Cy5-labeled pp-siRNA/siRNA (red) nanoplexes, with the nuclei and late endosomes/lysosomes stained with Hoechst 33342 (blue) and LysoTracker Green 488, respectively. The co-localization between the AT nanoplexes (red punctates) and lysosomes (green punctates) occurred at 4 hr and then continued to 8 hr, whereas the shared patterns between the MT nanoplexes and lysosomes appeared until 6 hr and then quickly faded away at 8 hr, as illustrated in Figure 6F. These results showed that MT nanoplexes, especially MT-pp-siRNA/CLDs, could enter into lysosomes later and escape from them earlier, which leads to the delivery of more siRNA drugs to the cytoplasm where RNAi occurred. This implies that pp-siRNA/CLDs produced using the MT preparation may have more efficiency for target mRNA inhibition compared with those produced via the AT method.

### Intracellular Degradation via the FRET Assay

A FRET-based method<sup>28,29</sup> uses biological probes to investigate intracellular degradation and dissociation of pp-siRNA and 3'-pS/pAs-siRNA conjugates in A375 cells. The Cy5 dye was linked at the 3' terminus of the antisense strand, and the Cy3 dye was linked at the 5' end of the sense strand. As seen from the confocal image (Figure 6C),  $I_{F(667)}$  showed the green dots, which represents the FRET signal obtained at 667 nm with an excitation at 561 nm, whereas the obtained signal of Cy3 excited at 561 nm [ $I_{F(570)}$ ] presented the red dots. Moreover, the ratiometric FRET data (Figure 6E) displayed that the degradation ratio of pp-siRNA was slower than that of others, which maintained the integrity until approximately 7 hr, whereas both siRNA and 3'-pAs-siRNA were dissociated at the 4-hr point.

### Target mRNA Inhibition *In Vitro*

The knockdown of B-Raf mRNA in A375 cells was detected via the RT-PCR analysis after transfection with four nanoplexes at three

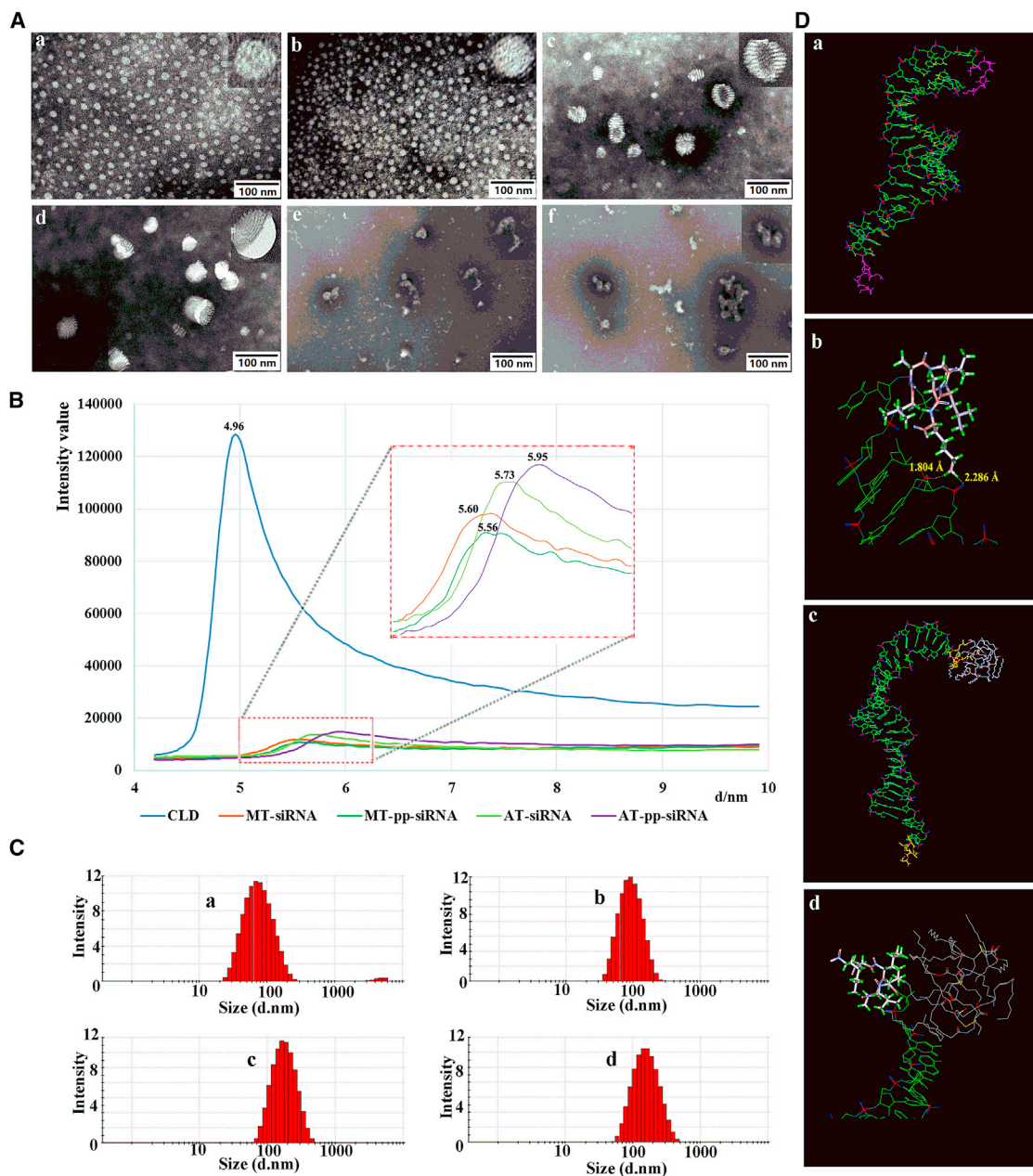


**Figure 2. Distinct Characterizations for the Nanoplexes of siRNA Conjugates/CLD**

(A) TEM morphologies of six nanoplexes of AT-pp-siMB3/CLDs (a), AT-siMB3/CLDs (b), MT-pp-siMB3/CLDs (c), MT-siRNA/CLDs (d), MT-3'-pAs-siMB3/CLDs (e), and MT-3'-pAs-siMB3/CLDs (f) at the ratio of N/P = 5/1. (B) SAXR results of CLD vesicles and four nanoplexes (MT-siRNA/CLDs, MT-pp-siRNA/CLDs, AT-siRNA/CLDs, and AT-pp-siRNA/CLDs). (C) DLS size distribution of AT-siRNA/CLDs (a), AT-pp-siRNA/CLDs (b), MT-siRNA/CLDs (c), and MT-pp-siRNA/CLDs (d). (D) Optimum configuration of pp-siRNA (a and b) and molecular dynamics simulation results of the complex formed by the dual interaction between pp-siRNA and CLDs (c and d).

concentrations of siRNA at different time points (Figure 4C). Generally, the tendency of target mRNA inhibition was dependent on both concentrations and times. At the same concentration, the level of downregulation was lower as time went by. Besides, at the same time point, the silencing efficiency was higher with increased concentrations. Under the condition of 100 nM

pp-siRNA/siRNA, there was significant inhibition (~50%–60%) of the target mRNA at 24 and 48 hr. Therefore, pp-siRNA presented an evident advantage in mRNA inhibition compared with siRNA in the same preparation. Significantly, at 48 and 72 hr, the MT-pp-siRNA/CLDs nanoplexes can more effectively decrease the mRNA expression.

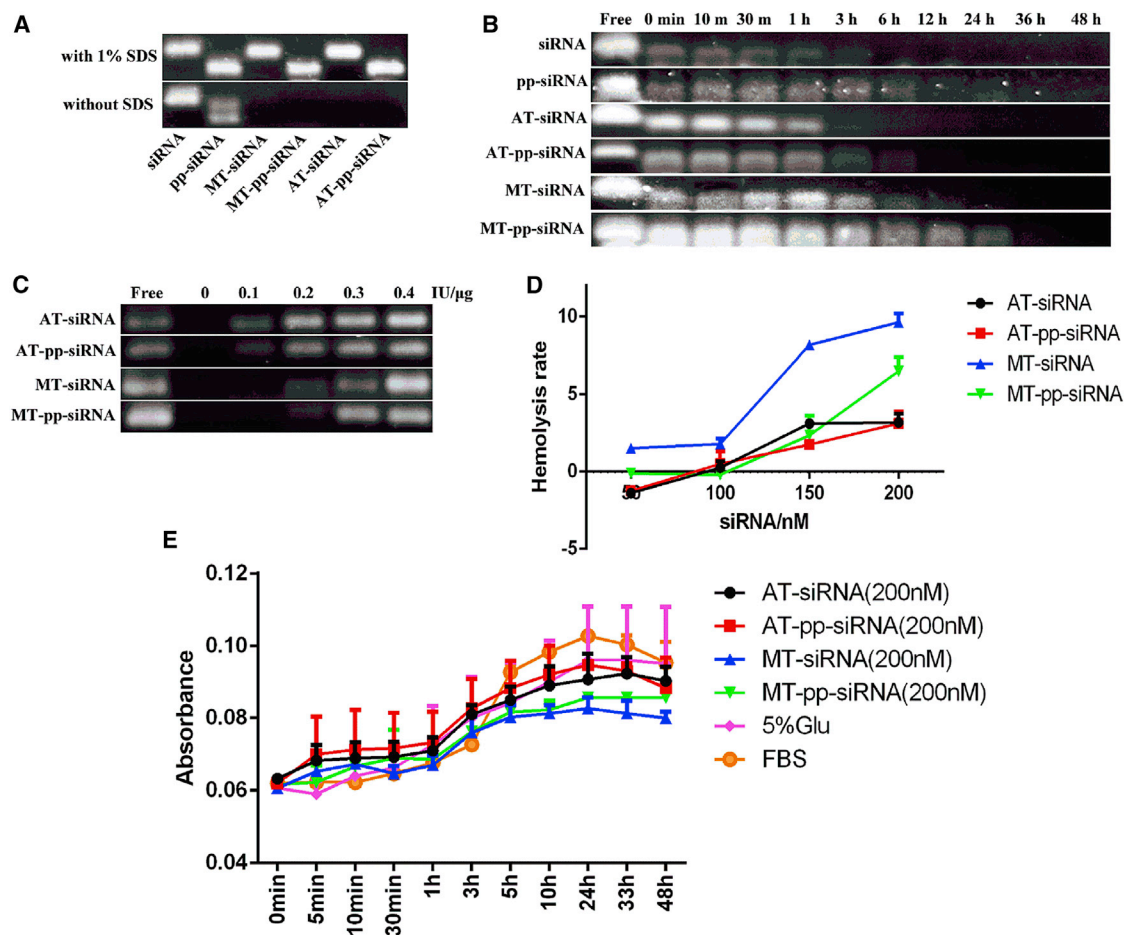


**Figure 3. In Vitro Evaluation of the Four Nanoplexes at N/P = 5/1**

(A) The capacity of nanoplex loading pp-siRNA/siRNA and integrity of siRNA (siRNA: 1 μM). (B) Protective effects in 50% FBS. (C) Stability against heparin displacement (heparin: IU/μg, siRNA: 100 nM). (D) Relative hemolysis effects at different concentrations of siRNA at 37°C. (E) The stability effects of serum with different nanoplex-loaded pp-siRNA/siRNA (200 nM) at different time points. All data are shown as the mean ± SD (n = 3).

The cell migration after the treatment of four nanoplexes was detected via the wound healing assay. Figure 4D shows the inhibition of migration: MT-pp-siRNA ≈ AT-pp-siRNA > AT-siRNA ≈ MT-siRNA, and the effect of gene knockdown is consistent with the RT-PCR result.

#### Tissue Distribution *In Vivo*

Investigation for drug accumulation in tumor tissue and other major organs is necessary for safety and effectiveness. In this study, Cy7-labeled pp-siRNA and siRNA were synthesized as a near-infrared fluorescence probe to be inserted into nanoplexes with CLDs. Biodistribution was observed via an *in vivo* imaging system after intravenous administration. As shown in Figure 7A, no fluorescent signal was detected in the control mice. After tail-vein injection, four nanoplexes were rapidly distributed to the major tissues. With time, the fluorescence intensity gradually decreased. As shown in Figure 7B, the nanoplexes were significantly accumulated in the liver at 12 hr and then were excreted out via renal clearance at 48 hr. In both the

tumor (Figure 7C) and other tissues (Figure 7B), a stronger fluorescence signal of pp-siRNA/CLDs was detected at the same time point than that of siRNA/CLDs via the same preparation, which suggested that pp-siRNA has a longer circulation time compared with siRNA. However, the fluorescence signals were primarily held in liver tissue from start to finish after intravenous injection.

#### Molecular Dynamic Simulation

The molecular dynamic simulation assay was performed to provide several auxiliary supports for the “dual interaction” between pp-siRNA and CLDs. The final conformational structure of pp-siRNA is shown in Figure 2Da. This structure presented the double-helix A-form conformation, similar to siRNA. Importantly, one of the six peptides at the 3' terminus was distorted by the hydrophobic segment (ALLAL), resulting in the stem-loop structure, where the amino group at the 3'-terminal end of lysine can bind to oxygen in 5'-phosphate groups of complementary strand via electrostatic force or hydrogen bonds (1.804 and 2.286 Å, Figure 2Db). This result

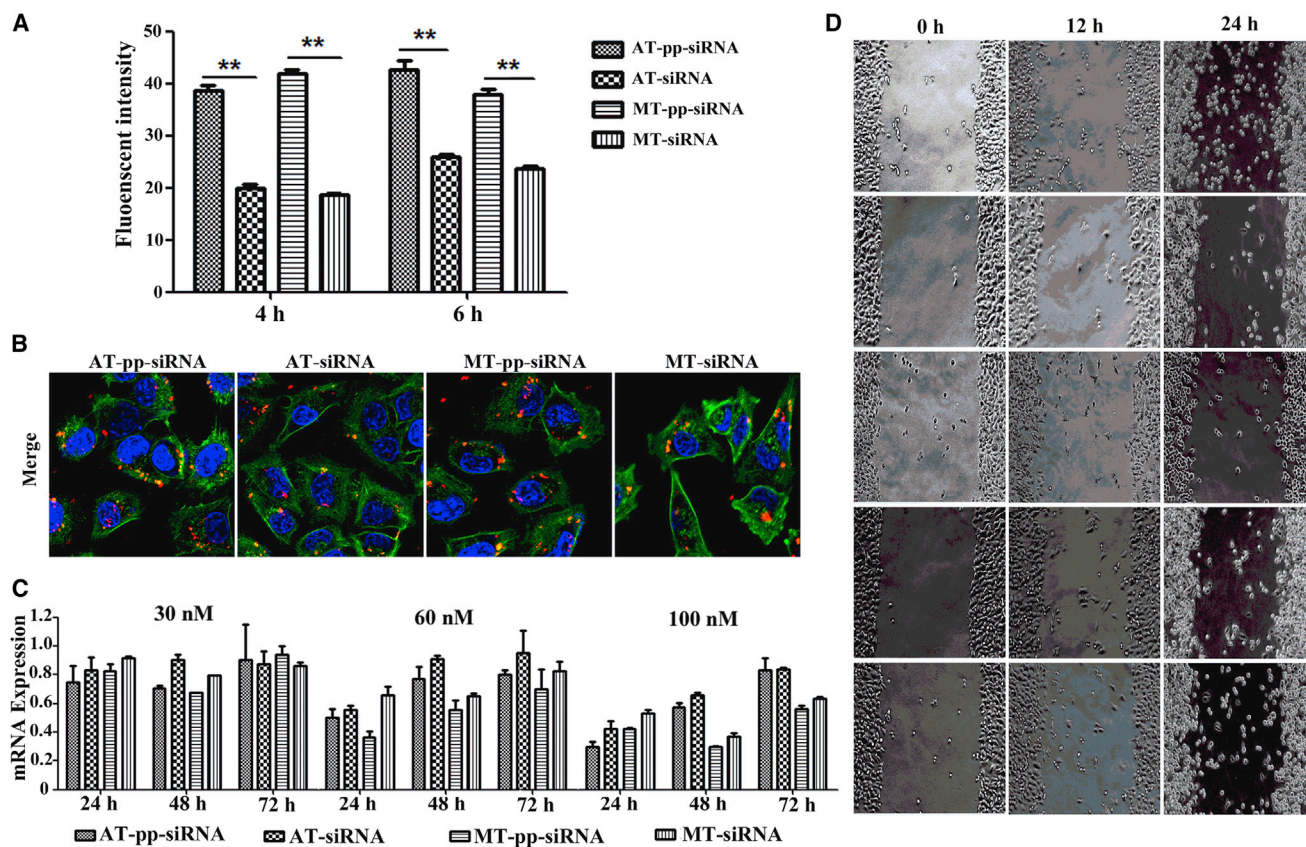


**Figure 4. Cellular Uptake and Its Application for the pp-siRNA/CLD Nanoparticle Therapy in Cultured Melanoma Cells**

(A) Intracellular fluorescence intensities were detected via flow cytometry after both 4- and 6-hr incubation with different nanoplexes at a 100 nM concentration. (B) Confocal microscopy after 4-hr incubation (the final concentration of Cy3-labeled pp-siMB3/siMB3 = 100 nM). The data are shown as the mean  $\pm$  SD ( $n = 3$ ).  $**p < 0.01$ . Hoechst 33258 (blue) and rhodamine-labeled phalloidin (green) were used to show the nucleus and membrane, respectively. (C) Relative expression of the targeted mRNA in A375 cells was treated with four nanoplexes loading pp-siRNA/siRNA against MB3 via RT-PCR at different concentrations (30, 60, and 100 nM) and at different times (24, 48, and 72 hr).  $n = 3$ .  $**p < 0.01$ . (D) Images of the A375 cell wound healing after being scratched for 12 or 24 hr.

implied that pp-siRNA may receive good protection from ribozyme degradation.

During the process of interaction between pp-siRNA and CLDs, the cap section at the 3' terminus of pp-siRNA was opened by the repulsion of the cationic regions in CLD molecules (Figure 2Dc), which were electrostatically absorbed by phosphate backbones to form the nanoplexes. Moreover, the hydrophobic segment of peptide was embedded into the domain composed of aliphatic alkanes in CLDs via the hydrophobic interaction (Figure 2Dd). These results displayed that bis-peptides can alter the mode of interaction between siRNA and CLDs by the extra hydrophobicity.

## DISCUSSION

Nanoparticles encapsulated with gene drugs need to undergo several bioprocesses (such as cellular uptake, intracellular trafficking, etc.) to perform silencing efficacy. Although every step can play a determinative effect on the targeted mRNA inhibition to some extent, the features of these nanoparticle nanostructures are regarded as funda-

mental.<sup>30</sup> Based on previous studies on siRNA conjugates, pp-siRNA was designed and considered as the "fixture" to anchor into the lipids' hydrophobic areas by bis-peptides, compared with the 3'-pep-siRNA conjugates. Hence, we employed pp-siRNA as a regulator in the assembly process of the nanoplexes by different preparation methods and then displayed these distinct intracellular fates. By engineering the nanocarrier architecture, the nanoplexes of MT-pp-siRNA/CLDs were shown to enhance the siRNA delivery.

Investigation of the assemblies' structures was one of the significantly important aspects for siRNA delivery.<sup>31,32</sup> An unambiguous frame of the optimized nanoplexes of pp-siRNA/CLDs has been revealed by a series of assays in this research. Taking all of the above-mentioned information, a structural hypothesis was proposed (Figure 8). After the cationic CLD vesicles were obtained by the AT preparation method, both pp-siRNA and siRNA were absorbed onto the surfaces of CLD vesicles, mainly by electrostatic interaction. During this time, the bis-peptides could not adequately interact with the hydrophobic sections of CLD liposomes, which implies that bis-peptides were

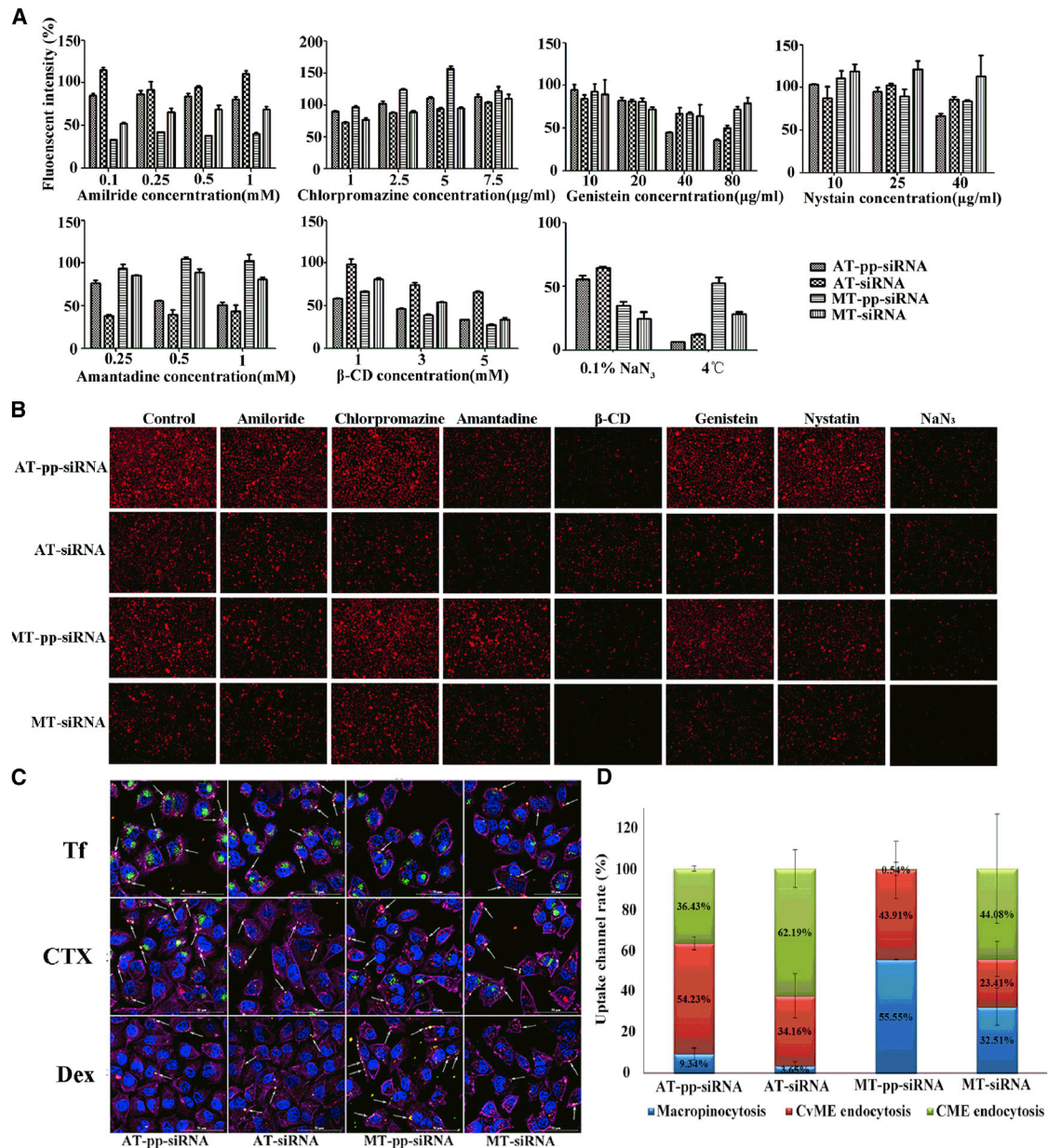


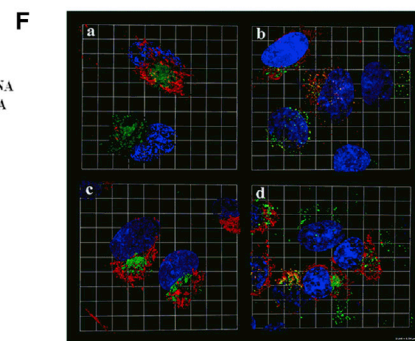
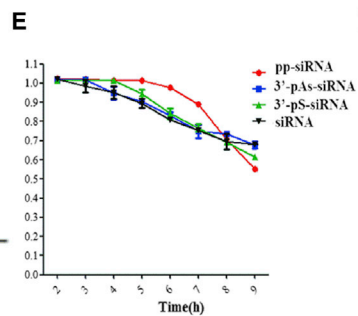
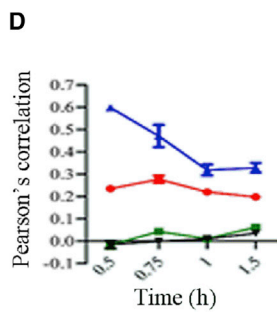
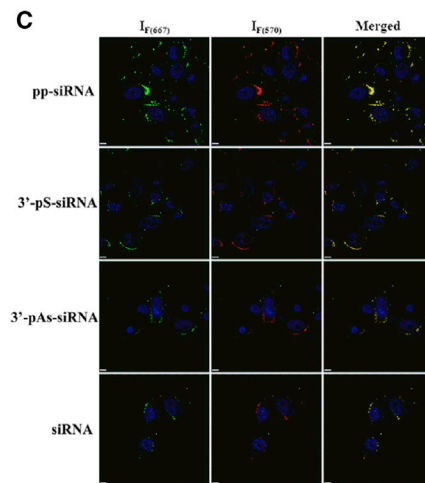
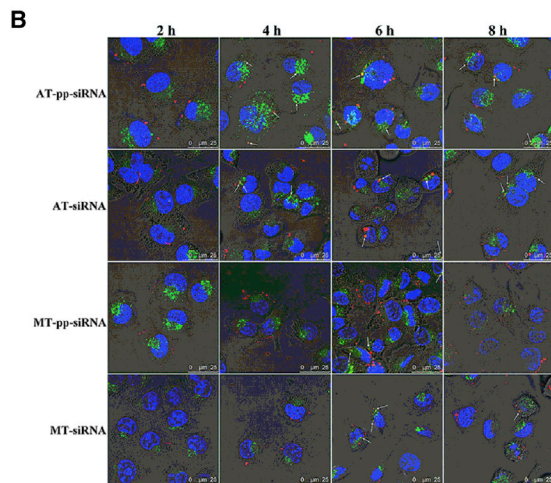
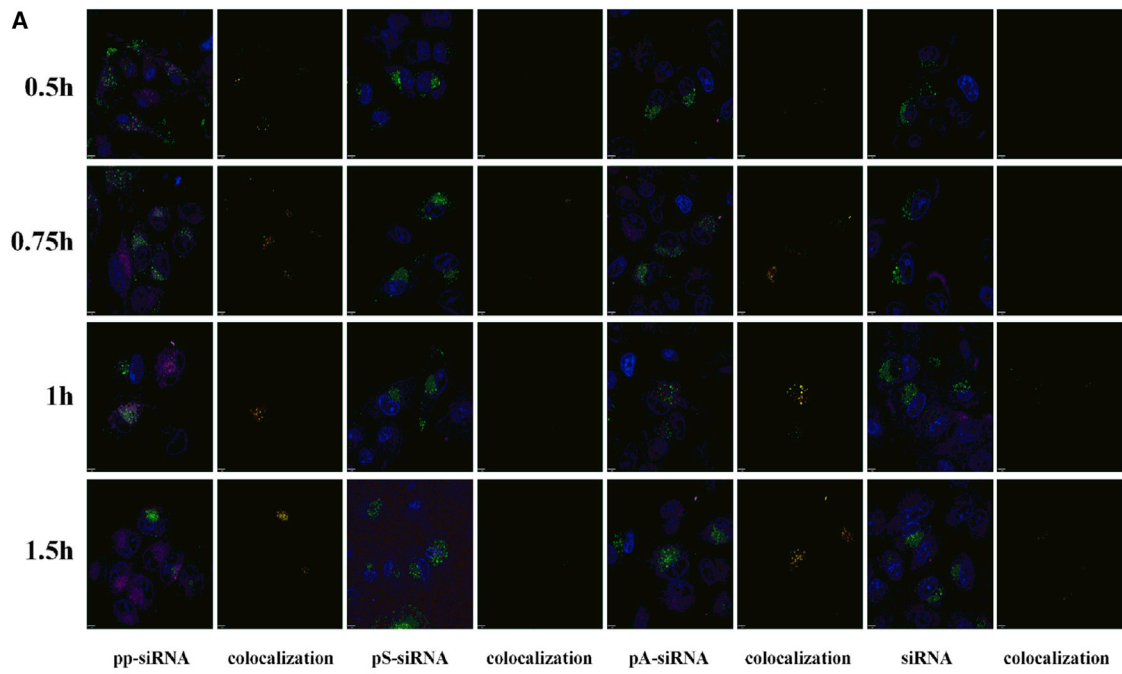
**Figure 5. Intracellular Pathway Investigation for Four Nanoplexes in A375 Cells after 4-hr Incubation**

(A) Cellular uptake with different pathway inhibitors was detected via flow cytometry. The mock (100%) was the fluorescent intensity without inhibitors ( $n = 3$ ). (B) Intracellular trafficking by fluorescence microscope. Inhibitors and their concentration: amiloride (0.5 mM), chlorpromazine (5  $\mu\text{g/ml}$ ), amantadine (1 mM),  $\beta$ -CD (5 mM), genistein (40  $\mu\text{g/ml}$ ), nystatin (40  $\mu\text{g/ml}$ ), and  $\text{NaN}_3$  (0.1%). (C) CLSM results of cellular pathways. Hoechst 33258 (blue) and rhodamine-labeled phalloidin (purple) were used to show the nucleus and membrane, respectively. The final concentration of Cy5-labeled pp-siRNA/siRNA (red) was 100 nM. Top row: Tf represented the transferrin from human serum. Middle row: CTXB represented as cholera toxin subunit B. Bottom row: Dex represented the dextran FITC conjugates. Green fluorescent signals were observed in the three substances. Yellow dots indicate co-localization (white arrows). (D) The channel ratio image of four nanoplexes in cellular uptake ( $n = 3$ ).

partially inserted into the vesicles and that other factors blocked the further contraction of the phosphate backbone with cationic regions. Finally, this process resulted in a similar morphology as spheroidal nanostructures (Figures 2Aa and 2Ab). However, both size parameters of pp-siRNA/CLDs (94.1 and 5.95 nm) were larger than those

of siRNA/CLDs (86.83 and 5.73 nm), and the zeta potential of pp-siRNA/CLDs (26.4 mV) was smaller than that of siRNA/CLDs (36.6 mV), as seen from Table 2 and Figure 2B. In the MT process, the bis-peptides of pp-siRNA played a key role in forming distinct assemblies. Once the CLD monomers were dropped into an siRNA





(legend on next page)

solution, they were reorganized along the pp-siRNA/siRNA backbones via electrostatic interaction, where the bis-peptides were thoroughly arranged into the hydrophobic region in the bilayers of CLDs. This organization assisted their self-assembly into nanoribbons, which were laterally associated and presented the distinct stripes. Finally, the hydrophobicity of bis-peptides helped accomplish the “close the loop,” producing ellipsoid-shaped nanostructures (Figure 2Ac) and more pyknotic monolayers (5.56 nm; Figure 2B). Although without the extra-hydrophobic force, the interactions between siRNAs and CLDs may not have promoted orderly “self-restraint,” which finally appeared as acalphe-like formations (Figure 2Ad) and a slightly loose monolayer (5.60 nm; Figure 2B).

The stability of nanoparticles is essential for siRNA protection. Observed from the nanostructures of four nanoplexes (Figures 2A and 8), each laminate was ~6 nm (Figure 2B). Moreover, the sizes of nanoplexes of both pp-siRNA and siRNA with CLD via the MT method (~150 nm; Table 2) were significantly larger than those via the AT preparation (~90 nm; Table 2; Figure 2C). These results mean that more laminate units (~25 layers) were composed in each MT particle than in AT formation (~5 layers). This implied that pp-siRNA/siRNA from MT nanoplexes (especially MT-pp-siRNA/CLDs) were more efficiently protected from degradation by nucleases and competition of negative proteins or polyoses, which was proven by the results of the serum protection assay (Figure 3B) and the assay of stability against heparin displacement (Figure 3C). All of these features stem from the special interaction between bis-peptides and lipids (Figure 2D), which also indicated that the peptide conjugation might alter the RISC loading process. In addition, the distinct nanostructures of four nanoplexes also suggested that they had biological specificity.

Currently, intracellular behavior is regarded as the key step in the cytosolic delivery of siRNA drugs.<sup>33</sup> Furthermore, cellular uptake pathways are considered vitally important in determining the efficiency of drugs as they relate to the intracellular trafficking and recycling of the internalized nanoplexes.<sup>34,35</sup> Generally, endocytosis is mainly divided into CME, CvME, macropinocytosis, and ATP-dependent endocytosis.<sup>36</sup> Because caveolae is a non-acidic degradative process, CvME has often been considered as the ideal uptake channel for drug delivery because it has the ability to bypass lysosomes. In addition, macropinosomes do not undergo the endosome process, which facilitates the drugs' rapid escape from lysosomes.<sup>37–39</sup> Several factors regulate the choice of endocytosis pathways, where the surface properties of nanoplexes play a critical role.<sup>40–42</sup> For the

distinct nanostructures, four nanoplexes should display their particular characteristics in uptake pathways, respectively. In the A375 cell line for malignant melanoma, two approaches were selected to elaborate the transmembrane mechanism. First, a series of pharmacological inhibitors (Table S2) that selectively inhibited CME, CvME, and macropinocytosis for determining the uptake pathway via reduction were observed by both FCM (Figure 5A) and fluorescence microscopy (Figure 5B). The concentrations of inhibitors were defined beforehand via the cellular viability assay (Figure S5). Second, several fluorescent-labeled trafficking pathway markers, such as transferrin, cholera toxin B (CTB), and dextran, were chosen to co-localize with Cy5-labeled nanoplexes via CLSM (Figure 5C). These results demonstrated that the nanoplexes of pp-siRNA/CLDs were taken up predominantly through CvME-mediated endocytosis and macropinocytosis (Figure 5D), especially by MT-pp-siRNA/CLDs. It was suggested that the bis-peptides linked to the 3' terminus of pp-siRNA can regulate multiple pathways to varying degrees. Importantly, this implied that the nanoplexes of MT-pp-siRNA/CLDs may mainly undergo non-acidification versus those of siRNA/CLDs, which should promote efficient release into the cytoplasm, leading to the efficient silencing activity for the target mRNA.

The reduction/avoidance of lysosomal degradation is considered to be paramount for the siRNA delivery. The prediction was that the nanoplexes of MT-pp-siRNA/CLDs can protect pp-siRNA from the lysosomal process and, finally, have the optimal gene silence. This dynamic process of lysosomal escape was observed via CLSM (Figures 6B and 6F), and it verified our above-mentioned conjecture. Significantly, the knockdown efficiency of MT-pp-siRNA presented an evident advantage compared with the three others at the same points via real-time PCR (60 and 100 nM, Figure 4C). Meanwhile, the intracellular stability of pp-siRNA and 3'-p-siRNA conjugates was probed via the FRET technology. Based on distance-dependent communication of the two dyes, it was an attractive way to better understand the dissociation and/or degradation state of siRNAs drugs, because the bio-behaviors resulted in spatial separation of the dyes and a disappearance of FRET.<sup>43,44</sup> In this study, the result (Figures 6C and 6E) presented higher intracellular sustainability of pp-siRNA than of others, which gave it more integrity in cells and implied that it may be able to efficiently silence the targeted mRNA. In addition, 3'-pS-siRNA was more slowly degraded than 3'-pAs-siRNA and siRNA. Several studies<sup>45</sup> for investigating the degradation of lipid-siRNA conjugated at the 3' end of the sense strand uncovered that Dicer nuclease can hydrolyze the conjugates into siRNA and then undergo the RNAi process.

#### Figure 6. Intracellular Distribution and Metabolism of Nanoplexes of siRNA Conjugates/CLDs

(A and D) Endosomal transport assay of MT-nanoplexes of 3'-pep-siMB3 conjugates/CLDs and siRNA/CLDs observed using CLSM (A) and its Pearson's correlation (D). (B) Lysosomal escape assay of four nanoplexes in A375 cells observed using CLSM. (C and E) Dissociation (C) and intracellular degradation (E) of pp-siRNA and 3'-pS/pAs-siRNA conjugates produced via the FRET technology. The Cy5 dye was linked at the 3' terminus of the antisense strand, and the Cy3 dye was linked at the 5' end of the sense strand.  $I_{F(667)}$  represents the FRET signal obtained at 667 nm with an excitation at 561 nm;  $I_{F(570)}$  represented the obtained signal of Cy3, which was excited at 561 nm. (F) Three-dimensional reconstruction image of the lysosomal escape assay of MT-pp-siRNA/CLDs (a, 6 hr; c, 8 hr) and AT-siRNA/CLDs (b, 6 hr; d, 8 hr) nanoplexes observed using CLSM. Hoechst 33258 (blue) and the LysoTracker Green DND-99 (green) were used to show the nucleus and endosomes, respectively. The final Cy5-labeled pp-siRNA/siRNA (red) concentration was 200 nM.

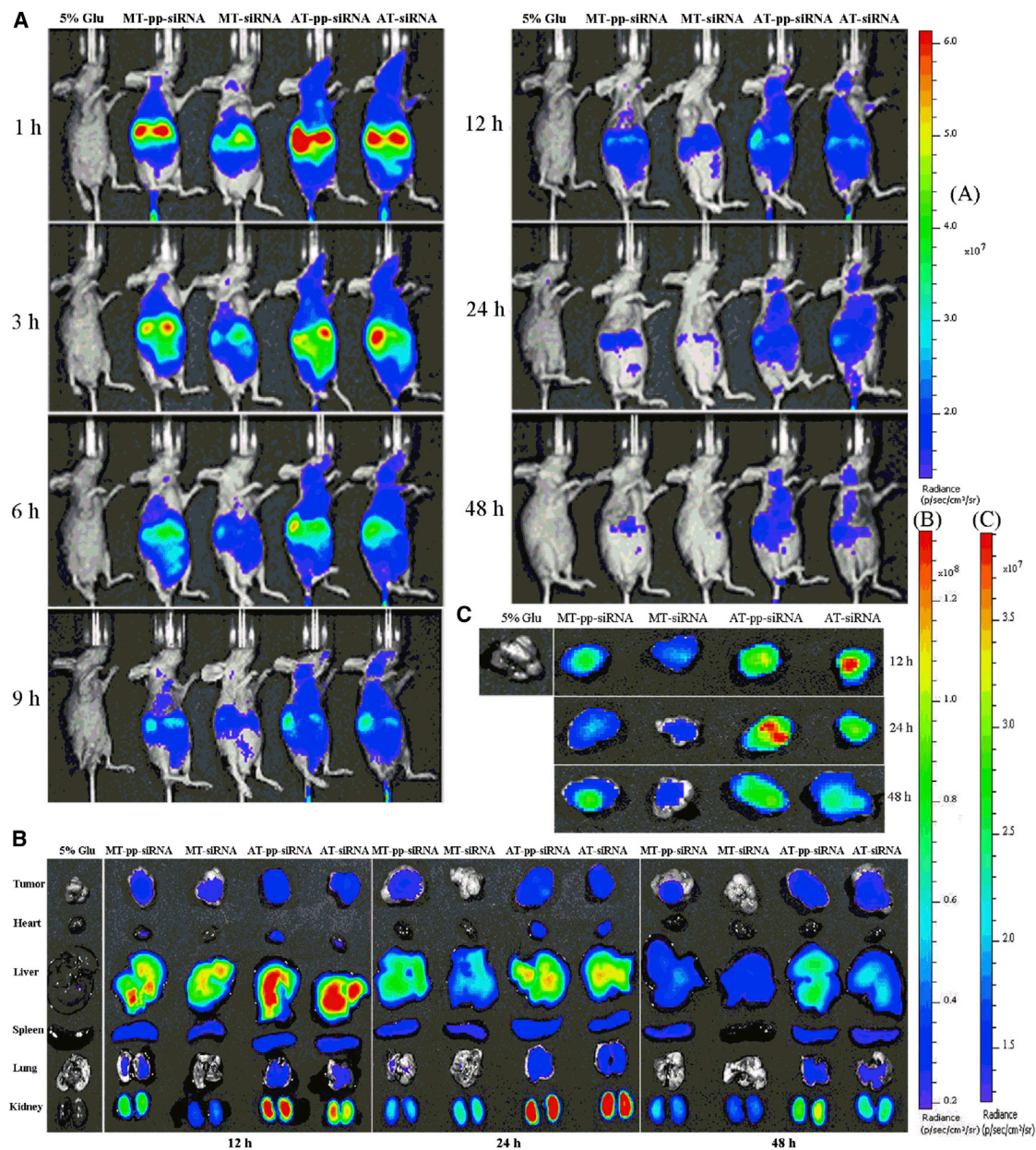


**Figure 7. In Vivo Tumor Tissue Accumulation and Circulation of Four Nanoplexes**

*In vivo* biodistribution of Cy7-labeled nanoplexes was observed via the CRI *in vivo* imaging system at the excitation wavelength of 745 nm and the emission wavelength of 800 nm. Nude mice bearing melanoma were given an intravenous injection via the tail vein. (A) Typical *in vivo* imaging. (B and C) *Ex vivo* imaging of organs (B) and tumor (C) excised from BALB/c nude mice. The concentrations of siRNAs were 1.0 mg/kg (N/P = 5/1).

Therefore, these results of the FRET assay implied that pp-siRNA may also suffer the Dicer recognition process, which improved the stability of pp-siRNA in cells at the same time point compared with others. These results demonstrate the superiority of MT-pp-siRNA/CLDs nanoplexes in intracellular behavior.

By regulating the assembly process and observing the intracellular fates of four nanoplexes, an intrinsic plotline in the story of siRNA

delivery process can be determined: the zeta potentials of nanoplexes of pp-siRNA/CLDs were lower than the ones of siRNA/CLDs (Table 2) in the same preparation approach. This feature meant that the nanoplexes of pp-siRNA/CLDs can predominantly internalize through the CME-independent pathways, because positively charged nanomedicines have usually undergone CME-mediated endocytosis.<sup>39</sup> In addition, the larger sizes of nanoplexes via the MT method suggested that macropinocytosis may be the main

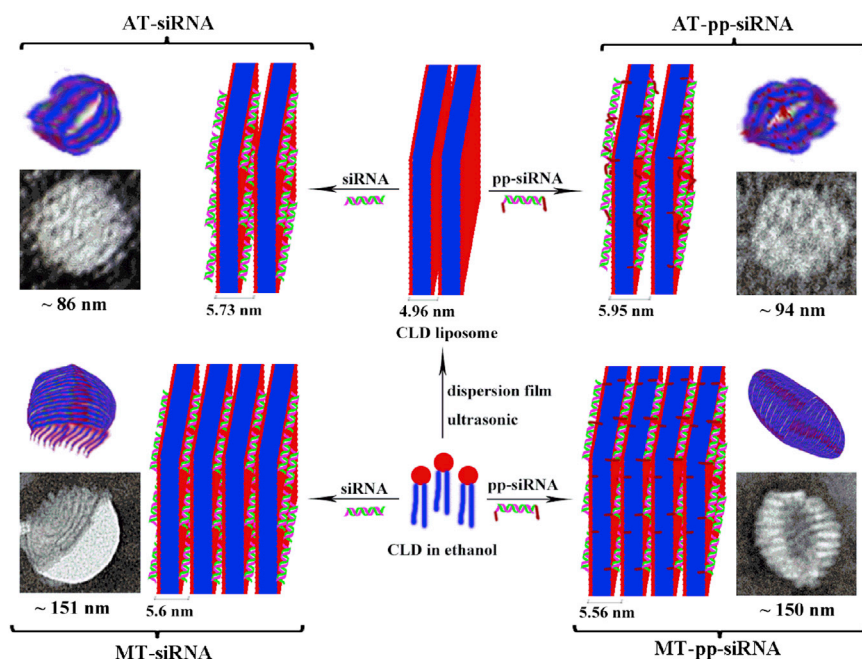


**Figure 8. Hypothesis of the Assembling Process Model of Four Nanoplexes between pp-siRNA/siRNA with CLDs**

A series of biological evaluations (such as cellular uptake, intracellular trafficking, degradation, RT-PCR, etc.) showed that the introduction of hydrophobic peptide (from siRNA to pp-siRNA) with a lower N/P ratio (5:1) and altering of the preparation method (from AT to MT) optimized the nanoplexes' structure, which gave siRNA a higher protection and furthermore regulated cellular pathways, then rapidly reached endosomes, and finally realized an effective escape from lysosomes and gene inhibition. Furthermore, the inner relationship of nanoplexes was clearly uncovered between the nanostructures and biofunctions. This is the first report that investigates the engineering of the nanocarrier architecture of 3',3''-bis-peptide-siRNA con-

jugates with CLDs, which opened up interesting avenues for the development of bis-molecular siRNA conjugates encapsulated by cationic vectors in siRNA therapeutics.

cellular entry channel.<sup>38</sup> Hence, based on altered nanostructures, it was speculated that the nanoplexes of MT-pp-siRNA/CLDs may enter cells through CvME-mediated endocytosis and macropinocytosis to a large extent (Figures 5C and 5D). Then, they bypass the lysosomes or quickly enact endosomal escape (Figure 6B), which finally resulted in high efficiency of the targeted mRNA inhibition (Figure 4C) and inhibited migration behavior (Figure 4D). All results supported our presumptions.

In addition, the *in vivo* biodistribution and tissue accumulation profiles of the pp-siRNA/CLD nanoplexes were clearly visualized (Figure 7). This showed that, in the same preparation methods, the pp-siRNA/CLDs nanoplexes had a longer circulation time (Figure 7A) and a relatively greater tumor accumulation (Figure 7C), which were attributed to their lower zeta potential, leading to reduced capture by the immune system and more stable aggregation for a longer half-time, compared with that of siRNA/CLDs. Meanwhile, the AT nanoplexes had more tumor accumulation because of their smaller size compared with the MT nanoplexes. However, there still were obvious imperfections: high accumulation was detected in both liver and kidneys during the entire period, and selective tumor accumulation did not effectively occur. These results may be explained by the composition of the vectors that were only amphiphilic lipids, readily captured by liver and kidneys in intravenous administration. Further study of targeting delivery and efficient inhibition *in vivo* will be reported in the near future.

In summary, our objective was to regulate the assembly structures of nanoplexes to alter their cellular pathways, which can improve the intracellular fates resulting in enhanced siRNA delivery.

## MATERIALS AND METHODS

### Materials and Cells

pp-siRNA/siRNA that targets mRNA of the mutant B-Raf protein (siMB3, antisense strand, 5'-GCU ACA GAG AAA UCU CGA Utdt-3', sense strand, 5'-AUC GAG AUU UCU CUG UAG Ctdt-3') was synthesized by our laboratories. The qPCR primer sequences of B-RAF were R (5'-ATG GGA CCC ACT CCA TCG AGA TTT CT-3') and F (5'-TGG TGT GAG GGC TCC AGC TTG T-3'). The CLDs were synthesized using the modified previously described methods. Cy3-N-hydroxysuccinimide (NHS), Cy5-NHS, and Cy7-NHS were purchased from QiweiTech (Beijing, China). 3'-PT-amino-modified controlled pore glass (CPG) was from Glen Research (Sterling, VA, USA). OPTI-MEM and LysoTracker DND-99 were purchased from Invitrogen (Grand Island, NY, USA); agarose was obtained from GENE Company (Hong Kong, China); Hoechst 33258 was purchased from Molecular Probes (Eugene, OR, USA); sulforhodamine B (SRB) was purchased from Sigma-Aldrich (St. Louis, MO, USA). Sodium chloride (NaCl), sodium phosphate dibasic (Na<sub>2</sub>HPO<sub>4</sub>), and hydroxyethyl piperazine ethanesulfonic acid (HEPES) were purchased from JandK Scientific (Beijing, China).

Human cervical carcinoma cells HeLa and human malignant melanoma cells A375 (Institute of Materia Medica, Chinese Academy of Medical Sciences and Peking Union Medical College, Beijing, China) were employed as *in vitro* assay models. All cells were grown continuously as a monolayer in DMEM in a humidified incubator at 37°C

and 5% CO<sub>2</sub>. DMEM was supplemented with 10% heat-inactivated FBS. The cells for all of the experiments were in the logarithmic phase of growth.

### Synthesis of siMB3 Conjugates and Fluorescent Samples

The general synthesis method for RNA samples was used, as described in previous studies.<sup>24,25</sup> In brief, oligonucleotides of siMB3 sequences were obtained using an ABI 394 DNA/RNA synthesizer using standard phosphoramidite chemistry with 3'-dT CPG, 3'-PT-amino-modified CPG (C6-CPG), and 3'-hexapeptide-modified CPG (KALLAL-CPG). After separation and purification, amino-modified single strands were reacted with various cyanine-NHS esters. Then, the fluorescence-labeled strands were purified via the Sephadex G-25 column. The purities of all single strands measured via high-performance liquid chromatography were >90%, and their identities were confirmed using MOLDI-TOF-MS. Finally, these complementary strands were annealed with an equivalent quality to form the corresponding siMB3 samples.

### Preparation Methods of the Nanoparticles

Four nanoplexes of pp-siRNA/CLDs and siRNA/CLDs were prepared using both thin-film hydration (AT)<sup>11</sup> and MT methods. After screening and optimization of the formulation, we confirmed the conditions of MT preparation. In brief, CLD monomers were dissolved in ethanol in a flask with an appropriate concentration (0.571 mg/mL) and then were dropped into the pp-siRNA/siRNA solution (5% glucose, 2 μM) under vibration with the volume ratio of CLD/siRNA (1:5). The mixture was subsequently sonicated at 70°C for 40 min, and ethanol was removed using a rotary evaporator. The CLD monomers and pp-siRNA/siRNA were mixed together with N/P = 5/1. For the AT preparation, CLD nanoplexes (5% glucose, 0.571 mg/mL) were dropped into the pp-siRNA/siRNA solution (5% glucose, 2 μM) under vibration with the volume ratio of CLD/siRNA (1:5). Then, the nanoplexes were incubated at 37°C for 20 min. As a result, four nanoplexes encapsulated by CLDs were obtained and diluted to a certain concentration for use.

### Sizes and Zeta Potentials Assay

The four nanoplexes were obtained using the AT and MT preparations. The particle sizes and zeta potentials were measured at 25°C using DLS (Malvern Zetasizer Nano ZS, Malvern, UK). The final concentration of siRNA was 100 nM.

### TEM

For the TEM analysis of the samples, the samples (100 nM, 10 μL) were applied on a copper grid and incubated for 1 min followed by removing excess solution with filter paper and then adding a 10 μL of staining solution (2% uranyl acetate; Sigma-Aldrich) for 2 min. After wicking away the staining solution, the sample grids were placed in a desiccator to dry under vacuum overnight. A JOEL 100CX transmission electron microscope was used to image the samples at 100 kV.

### SAXR

The freshly prepared four nanoplexes at the N/P = 5/1 ratio were frozen and dried in a lyophilizer to yield a white powder for SAXR. The samples were put into an aluminum sample holder with a 5-mm-hole diameter and sealed with Kapton tape. The working voltage and current for the X-ray tube are 45 kV and 0.88 mA, respectively. The X-ray wavelength was 0.154 nm. The scattering vector (*q*) was calibrated using silver behenate with the primary reflection peak at  $q = 1.067 \text{ nm}^{-1}$ . The SAXS diffraction patterns covering the *q* range between 0.2 and 2.0 nm<sup>-1</sup> were recorded. The background scattering was subtracted and further analyzed using the Rigaku SAXSgui software.

### Gel Retardation Assay

Four nanoplexes of pp-siRNA/CLDs and siRNA/CLDs were prepared at the N/P = 5/1 ratios, as described above. The final pp-siRNA/siRNA concentration was fixed at 1 μM. These nanoplexes were approached with a loading buffer, or a loading buffer containing 1% SDS, and electrophoresed on a 1% agarose gel containing 0.5 mg/mL Exred. Electrophoresis was performed at 80 mV for 3 min, then subsequently 100 mV for 10 min. The resulting gels were photographed under UV illumination. Free pp-siRNA or siRNA was used as the control.

To analyze the protective effect of four nanoplexes on pp-siRNA/siRNA, an equal volume mix of nanoplexes (siRNA 2.4 μM) with FBS was incubated at 37°C. Then, a set sample was kept at -20°C. Finally, a gel retardation assay was applied to all samples.

### Cellular Uptake Efficiency Assay

A375 cells were seeded  $2.5 \times 10^5$  per well in six-well plates. After 24-hr proliferation, four nanoplexes containing Cy3-labeled pp-siRNA/siRNA with N/P = 5/1 at the fixed final concentration of 100 nM were exposed to the cells and incubated for an additional 4 or 6 hr at 37°C. After incubation, the cells were harvested and washed three times with a pre-cooled PBS solution, and the uptake of Cy3-labeled pp-siRNA/siRNA was immediately detected using a FACSCalibur flow cytometer (Becton Dickinson, San Jose, CA, USA). Meanwhile, the fluorescence distribution of cells after 4 hr was visualized using a Leica TCS SP8 confocal fluorescence microscope (Leica Microsystems, Heidelberg, Germany).

### Endocytotic Pathway Assay

A375 cells were plated in 12-well tissue culture plates at  $2 \times 10^5$  cells/well 24 hr prior to transfection. For the transfections performed in the presence of various concentrations of different inhibitors (genistein, chlorpromazine, amiloride, amantadine, β-CD, nystatin, and NaN<sub>3</sub>), or at 4°C, the growth medium was replaced with a serum-free medium containing the desired drug 30 min prior to transfection. Then, four nanoplexes containing Cy3-labeled pp-siRNA/siRNA with N/P = 5/1 at the fixed final concentration of 100 nM were exposed to the cells and incubated for an additional 4 hr at 37°C or 4°C. In the process of incubation, the concentration of inhibitors or temperature was consistent with the pretreatment. After incubation, the cells were harvested and washed three times with pre-cooled PBS solution, and the uptake of Cy3-labeled pp-siRNA/siRNA was

detected using a FACSCalibur flow cytometer (Becton Dickinson) or an inverted fluorescence microscope (Leica Microsystems) immediately.

Confocal microscopy was also used to observe the channels of cellular uptake of four nanoplexes. A375 cells were plated in confocal dishes (15 mm) at  $2 \times 10^5$  cells/well 24 hr prior to transfection. Then, various formulations containing Cy5-labeled pp-siRNA/siRNA with N/P = 5/1 at the fixed final concentration of 200 nM were exposed to cells and incubated for an additional 1 hr at 37°C. Before the end of incubation, Tf (transferrin from human serum, Alexa Fluor 488 conjugate, 10 µg/mL for 10 min), CTB (cholera toxin subunit B, Alexa Fluor 488 conjugates, 2 µg/mL for 30 min), and dextran (dextran FITC conjugates, 1 mg/mL for 1 hr) were added into the incubation system. After transfection, the cells were washed three times with PBS followed by fixation with 4% paraformaldehyde for 15 min and cell punching with 0.1% Triton-PBS for 1 min at room temperature. Then, F-actin filaments and nuclei were individually stained with rhodamine-labeled phalloidin (1 U/mL for 10 min) and Hoechst 33258 (5 µg/mL for 10 min), as per the manufacturer's instructions. Cells were visualized under a Leica TCS SP8 confocal fluorescence microscope (Leica Microsystems).

#### Lysosome Escape Assay

A375 cells ( $2 \times 10^5$  cells/well) were seeded into confocal dishes. After 24-hr incubation, four nanoplexes of Cy5-labeled pp-siRNA/siRNA with CLDs (200 nM) were added into each dish for different time periods. At the end of transfection, LysoTracker Green (Invitrogen, Carlsbad, CA, USA) (500 nM) was added to the medium and incubated with the cells for 30 min at 37°C for endosome/lysosome labeling. Next, the cells were washed with PBS three times. Intracellular distribution of Cy5-labeled pp-siRNA/siRNA was observed with a Leica SP 8 confocal microscope (Leica Microsystems).

#### Intracellular Degradation Analysis via the FRET Technology

Fluorescent-labeled pp-siRNA was utilized with both a cyanine-5 dye at the 3' terminus of the guide strand and a cyanine-3 dye at the 5' terminus of the sense strand. A375 cells ( $2 \times 10^5$  cells/well) were seeded in a chambered glass plate for 36 hr. In total, 500 µL of the serum-free media containing pp-siRNA/CLD, 3'-pAs-siRNA/CLD, 3'-pS-siRNA/CLD, and siRNA/CLD nanoplexes produced using the MT preparation (100 nM) was added to each well and incubated for 2 hr at 37°C. After being transfected with these nanoplexes, the cells were washed with a PBS solution three times, and a serum-containing media was added. Real-time confocal images were taken using an UltraVIEW VoX inverted confocal laser scanning microscope (PerkinElmer, USA). Each sample was excited at 561 nm to acquire the fluorescence signal of cyanine-3 (emission: 570 nm). The fluorescence signal of Cy5-labeled pp-siRNA/siRNA can be detected at 670 nm with an excitation at 641 nm. The FRET signal was obtained at 670 nm with an excitation at 561 nm. The merged image and data analysis were processed using the Volocity 6.2.1 software.

#### In Vitro Gene Silencing Assay

The levels of mRNA in the cells treated with different nanoparticles (N/P = 5/1, final siRNA concentrations were 30, 60, and 100 nM) were analyzed via RT-PCR. To detect the relative B-RAF mRNA expression, we seeded A375 cells ( $1.5 \times 10^5$  cells/well) into 12-well tissue culture plates. After 24-hr proliferation, various formulations containing siMB3 with N/P = 5/1 at the fixed different final concentration were exposed to cells and incubated for an additional 6 hr at 37°C. Then, the cells underwent another 24, 48, and 72 hr of incubation. Total RNA was extracted using the TRIOL reagent method and reverse transcribed using a GoScript Reverse Transcription System (A5001; Promega, Madison, WI, USA). The resulting cDNAs were used for PCR using a GoTaq qPCR Master Mix (A6002; Promega) in triplicates. PCR and data collection were performed on a real-time PCR amplifier (MX3005P; Stratagene, La Jolla, CA, USA). All quantitations were normalized to an endogenous control of reduced glyceraldehyde-phosphate dehydrogenase (GAPDH). The relative quantitation value for each target gene compared with the calibrator for that target was expressed as  $2^{-(Ct-Cc)}$  (Ct and Cc were the mean threshold cycle differences after normalizing to GAPDH).

#### In Vivo Distribution

Each of the  $2 \times 10^6$  A375 cells was inoculated into the right armpit of each BALB/c female nude mouse to establish the *in situ* melanoma model. When tumor size reached 500 mm<sup>3</sup>, the mice were administered with nanoplexes (Cy7-labeled siRNA 1 mg/kg) via the tail vein, and the fluorescence distribution was visualized at the predetermined time points *in vivo* using an imaging system (Imaging Station Maestro 2; CRI, MA, USA) with the excitation wavelength of 745 nm and emission wavelength of 800 nm. Tumor and major organs, including heart, liver, spleen, lung, and kidney, were excised and imaged. All images were normalized and analyzed using the Imaging Station Maestro 2 software. All procedures involving experimental animals were performed in accordance with protocols approved by the Committee for Animal Research of Peking University, China and conformed to the Guide for the Care and Use of Laboratory Animals.

#### Molecular Dynamics Simulation

Molecular dynamics (MD) simulation was performed using the AMBER 11 molecular simulation package. The ff99SB force field was used to describe the special conformation of pp-siRNA and the interaction between pp-siRNA and CLDs. The model was solvated in TIP3P water using an octahedral box, which extended 15 Å away from any solute atom. Na<sup>+</sup> counterion was placed next to each phosphate group to neutralize the negative charges of simulated molecules.

The calculations began with 500 steps of the steepest descent followed by 500 steps of conjugate gradient minimization with a large constraint of 500 kcal mol<sup>-1</sup> Å<sup>-2</sup> on pp-siRNA and the complexes of pp-siRNA/CLDs. Then, 1,000 steps of the steepest descent followed by 1,500 steps of conjugate gradient minimization were performed, with no restraints on pp-siRNA and the complexes of pp-siRNA/CLDs. Subsequently, after 20 ps of MD, during which the temperature

was slowly raised from 0 to 300 K, with weak ( $10 \text{ kcal mol}^{-1} \text{ \AA}^{-2}$ ) restraints on the pp-siRNA and the complexes of pp-siRNA/CLDs, the final unrestrained production simulations of 3.0 ns for the molecule were carried out at constant pressure (1 atm) and temperature (300 K). In the entire simulation, SHAKE was applied to all hydrogen atoms. Periodic boundary conditions with minimum image conventions were applied to calculate the non-bonded interactions. A cutoff of 10 Å was used for the Lennard-Jones interactions. The final structures were produced from the 1,000 steps of minimized averaged structure of the last 20 ns of MD.

### Statistical Analysis

For statistical analysis between the two groups, Student's t test for independent means was applied. The differences between any two groups out of several groups were analyzed via one-way analysis of variance (ANOVA) followed by least significant difference (LSD) multiple comparisons. Statistical analysis was performed using the SPSS software (version 16.0; SPSS, Chicago, IL, USA).

### SUPPLEMENTAL INFORMATION

Supplemental Information includes Supplemental Materials and Methods, five figures, two schemes, and two tables and can be found with this article online at <https://doi.org/10.1016/j.omtn.2017.11.002>.

### AUTHOR CONTRIBUTIONS

Conceptualization: Z.Y. and J.W.; Design, Analysis and Writing: J.S.; Major Biological Experiments: C.Q. and W.W.; Supplementary Experiments: Y.D. and H.J.; Constructive Discussions: L.Z. and Y.Z.

### ACKNOWLEDGMENTS

This work was supported by the Ministry of Science and Technology of China (grants 2012AA022501, 2012CB720604, and 2013CB932501) and the National Natural Science Foundation of China (grants 20932001, 81302626, 81273455, and 81473158). In addition, we thank Prof. D.S. Guo and Prof. Y. Chen in Yu Liu's group at the Department of Chemistry of Nankai University for providing the constructive comments on experiments for supramolecular characterization.

### REFERENCES

- Haussecker, D., and Kay, M.A. (2015). RNA interference. *Drugging RNAi*. *Science* 347, 1069–1070.
- Wu, S.Y., Lopez-Berestein, G., Calin, G.A., and Sood, A.K. (2014). RNAi therapies: drugging the undruggable. *Sci. Transl. Med.* 6, 240ps7.
- Coelho, T., Adams, D., Silva, A., Lozeron, P., Hawkins, P.N., Mant, T., Perez, J., Chiesa, J., Warrington, S., Tranter, E., et al. (2013). Safety and efficacy of RNAi therapy for transthyretin amyloidosis. *N. Engl. J. Med.* 369, 819–829.
- Haussecker, D. (2014). Current issues of RNAi therapeutics delivery and development. *J. Control. Release* 195, 49–54.
- Jones, C.H., Chen, C.K., Ravikrishnan, A., Rane, S., and Pfeifer, B.A. (2013). Overcoming nonviral gene delivery barriers: perspective and future. *Mol. Pharm.* 10, 4082–4098.
- Zhang, J., Li, X., and Huang, L. (2014). Non-viral nanocarriers for siRNA delivery in breast cancer. *J. Control. Release* 190, 440–450.
- Sarett, S.M., Nelson, C.E., and Duvall, C.L. (2015). Technologies for controlled, local delivery of siRNA. *J. Control. Release* 218, 94–113.
- Kim, H.J., Kim, A., Miyata, K., and Kataoka, K. (2016). Recent progress in development of siRNA delivery vehicles for cancer therapy. *Adv. Drug Deliv. Rev.* 104, 61–77.
- Stewart, M.P., Sharei, A., Ding, X., Sahay, G., Langer, R., and Jensen, K.F. (2016). In vitro and ex vivo strategies for intracellular delivery. *Nature* 538, 183–192.
- Barrán-Berdón, A.L., Muñoz-Úbeda, M., Aicart-Ramos, C., Pérez, L., María-Rosa, L., Castro-Hartmann, P., Martín-Molina, A., Aicart, E., and Elena Junquera, E. (2012). Ribbon-type and cluster-type lipoplexes constituted by a chiral lysine based cationic gemini lipid and plasmid DNA. *Soft Matter* 8, 7368–7380.
- Kirby, A.J., Camilleri, P., Engberts, J.B., Feiters, M.C., Nolte, R.J., Söderman, O., Bergsma, M., Bell, P.C., Fielden, M.L., García Rodríguez, C.L., et al. (2003). Gemini surfactants: new synthetic vectors for gene transfection. *Angew. Chem. Int. Ed. Engl.* 42, 1448–1457.
- Ghanbari Safari, M., and Hosseinkhani, S. (2013). Lipid composition of cationic nanoliposomes implicate on transfection efficiency. *J. Liposome Res.* 23, 174–186.
- Shim, G., Han, S.E., Yu, Y.H., Lee, S., Lee, H.Y., Kim, K., Kwon, I.C., Park, T.G., Kim, Y.B., Choi, Y.S., et al. (2011). Trilysinoyl oleylamide-based cationic liposomes for systemic co-delivery of siRNA and an anticancer drug. *J. Control. Release* 155, 60–66.
- Tseng, Y.C., Mozumdar, S., and Huang, L. (2009). Lipid-based systemic delivery of siRNA. *Adv. Drug Deliv. Rev.* 61, 721–731.
- Hatakeyama, H., Akita, H., and Harashima, H. (2011). A multifunctional envelope type nano device (MEND) for gene delivery to tumours based on the EPR effect: a strategy for overcoming the PEG dilemma. *Adv. Drug Deliv. Rev.* 63, 152–160.
- Sakurai, Y., Hatakeyama, H., Sato, Y., Hyodo, M., Akita, H., and Harashima, H. (2013). Gene silencing via RNAi and siRNA quantification in tumor tissue using MEND, a liposomal siRNA delivery system. *Mol. Ther.* 21, 1195–1203.
- Chen, Y., Bathula, S.R., Li, J., and Huang, L. (2010). Multifunctional nanoparticles delivering small interfering RNA and doxorubicin overcome drug resistance in cancer. *J. Biol. Chem.* 285, 22639–22650.
- Li, S.D., and Huang, L. (2006). Surface-modified LPD nanoparticles for tumor targeting. *Ann. N Y Acad. Sci.* 1082, 1–8.
- Feng, Q., Yu, M.Z., Wang, J.C., Hou, W.J., Gao, L.Y., Ma, X.F., Pei, X.W., Niu, Y.J., Liu, X.Y., Qiu, C., et al. (2014). Synergistic inhibition of breast cancer by co-delivery of VEGF siRNA and paclitaxel via vaporeotide-modified core-shell nanoparticles. *Biomaterials* 35, 5028–5038.
- Deng, Z.J., Morton, S.W., Ben-Akiva, E., Dreaden, E.C., Shopsowitz, K.E., and Hammond, P.T. (2013). Layer-by-layer nanoparticles for systemic codelivery of an anticancer drug and siRNA for potential triple-negative breast cancer treatment. *ACS Nano* 7, 9571–9584.
- Ma, X.F., Sun, J., Qiu, C., Wu, Y.F., Zheng, Y., Yu, M.Z., Pei, X.W., Wei, L., Niu, Y.J., Pang, W.H., et al. (2016). The role of disulfide-bridge on the activities of H-shape gemini-like cationic lipid based siRNA delivery. *J. Control. Release* 235, 99–111.
- Zheng, Y., Guo, Y.J., Li, Y.T., Wu, Y., Zhang, L.H., and Yang, Z.J. (2014). A novel gemini-like cationic lipid for the efficient delivery of siRNA. *New J. Chem.* 38, 4952–4962.
- Wang, X.F., Huang, Y., Liu, Y., Chen, Y., Jin, H.W., Zheng, Y., Du, Q., Yang, Z.J., and Zhang, L.H. (2013). Synthesis and biological evaluation of peptide-siRNA conjugates with phosphodiester unit as linker. *Sci. China Chem.* 56, 1542–1549.
- Liu, Y., Wang, X.F., Chen, Y., Zhang, L.-H., and Yang, Z.-J. (2012). A solid-phase method for peptide-siRNA covalent conjugates based on click chemistry. *Med. Chem. Comm.* 3, 506–511.
- Zou, L., and Yang, Z.J. (2014). Serum stability enhancement of siRNA caused by peptide conjugation at 3' terminus of sense strand. *J. Chin. Pharm. Sci.* 23, 215–219.
- Fan, X., Zhang, Y., Liu, X., He, H., Ma, Y., Sun, J., Huang, Y., Wang, X., Wu, Y., Zhang, L., and Yang, Z. (2016). Biological properties of a 3',3''-bis-peptide-siRNA conjugate in vitro and in vivo. *Bioconjug. Chem.* 27, 1131–1142.
- Pratilas, C.A., Taylor, B.S., Ye, Q., Viale, A., Sander, C., Solit, D.B., and Rosen, N. (2009). (V600E)BRAF is associated with disabled feedback inhibition of RAF-MEK signaling and elevated transcriptional output of the pathway. *Proc. Natl. Acad. Sci. USA* 106, 4519–4524.

28. Jiang, S., and Zhang, Y. (2010). Upconversion nanoparticle-based FRET system for study of siRNA in live cells. *Langmuir* 26, 6689–6694.
29. Alabi, C.A., Love, K.T., Sahay, G., Stutzman, T., Young, W.T., Langer, R., and Anderson, D.G. (2012). FRET-labeled siRNA probes for tracking assembly and disassembly of siRNA nanocomplexes. *ACS Nano* 6, 6133–6141.
30. Rao, C.N., and Biswas, K. (2009). Characterization of nanomaterials by physical methods. *Annu. Rev. Anal. Chem. (Palo Alto, Calif.)* 2, 435–462.
31. Ni, R., and Chau, Y. (2014). Structural mimics of viruses through peptide/DNA co-assembly. *J. Am. Chem. Soc.* 136, 17902–17905.
32. Liu, H., Li, Y., Mozhi, A., Zhang, L., Liu, Y., Xu, X., Xing, J., Liang, X., Ma, G., Yang, J., and Zhang, X. (2014). siRNA-phospholipid conjugates for gene and drug delivery in cancer treatment. *Biomaterials* 35, 6519–6533.
33. Martens, T.F., Remaut, K., Demeester, J., De Smedt, S.C., and Braeckmans, K. (2014). Intracellular delivery of nanomaterials: How to catch endosomal escape in the act. *Nano Today* 9, 344–364.
34. Juliano, R., Alam, M.R., Dixit, V., and Kang, H. (2008). Mechanisms and strategies for effective delivery of antisense and siRNA oligonucleotides. *Nucleic Acids Res.* 36, 4158–4171.
35. Wang, Y., and Huang, L. (2013). A window onto siRNA delivery. *Nat. Biotechnol.* 31, 611–612.
36. Doherty, G.J., and McMahon, H.T. (2009). Mechanisms of endocytosis. *Annu. Rev. Biochem.* 78, 857–902.
37. Alam, M.R., Ming, X., Fisher, M., Lackey, J.G., Rajeev, K.G., Manoharan, M., and Juliano, R.L. (2011). Multivalent cyclic RGD conjugates for targeted delivery of small interfering RNA. *Bioconjug. Chem.* 22, 1673–1681.
38. Sahay, G., Alakhova, D.Y., and Kabanov, A.V. (2010). Endocytosis of nanomedicines. *J. Control. Release* 145, 182–195.
39. Hillaireau, H., and Couvreur, P. (2009). Nanocarriers' entry into the cell: relevance to drug delivery. *Cell. Mol. Life Sci.* 66, 2873–2896.
40. McLendon, P.M., Fichter, K.M., and Reineke, T.M. (2010). Poly(glycoamidoamine) vehicles promote pDNA uptake through multiple routes and efficient gene expression via caveolae-mediated endocytosis. *Mol. Pharm.* 7, 738–750.
41. Zhu, X.D., Zhuang, Y., Ben, J.J., Qian, L.L., Huang, H.P., Bai, H., Sha, J.H., He, Z.G., and Chen, Q. (2011). Caveolae-dependent endocytosis is required for class A macrophage scavenger receptor-mediated apoptosis in macrophages. *J. Biol. Chem.* 286, 8231–8239.
42. Rejman, J., Oberle, V., Zuhorn, I.S., and Hoekstra, D. (2004). Size-dependent internalization of particles via the pathways of clathrin- and caveolae-mediated endocytosis. *Biochem. J.* 377, 159–169.
43. Alabi, C.A., Sahay, G., Langer, R., and Anderson, D.G. (2013). Development of siRNA-probes for studying intracellular trafficking of siRNA nanoparticles. *Integr. Biol.* 5, 224–230.
44. Roy, R., Hohng, S., and Ha, T. (2008). A practical guide to single-molecule FRET. *Nat. Methods* 5, 507–516.
45. Kubo, T., Takei, Y., Mihara, K., Yanagihara, K., and Seyama, T. (2012). Amino-modified and lipid-conjugated dicer-substrate siRNA enhances RNAi efficacy. *Bioconjug. Chem.* 23, 164–173.